Superior protection by α-Al2O3/α-LiAlO2 double oxide scales against alkali carbonate corrosion

Corrosion Science 218 (2023) 111217

Contents lists available at ScienceDirect

Corrosion Science

journal homepage: www.elsevier.com/locate/corsci

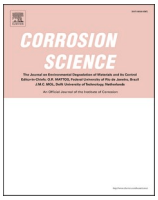

Superior protection by α-Al_2O_3/α-$LiAlO_2$ double oxide scales against alkali carbonate corrosion

Esraa Hamdy [a,*], Fang Liu [b], Christine Geers [a]

[a] Department of Chemistry and Chemical Engineering, Chalmers University of Technology, Gothenburg SE-412 96, Sweden
[b] Department of Industrial and Materials Science, Chalmers University of Technology, Gothenburg SE-412 96, Sweden

ARTICLE INFO

Keywords:
Lithium aluminate
Pre-oxidation, Alumina forming alloys
Molten salt
High-temperature corrosion
Phase transition

ABSTRACT

Ferritic alumina-forming alloys showed high corrosion resistance to molten carbonates by forming a protective α-$LiAlO_2$ scale at their surface. In this work, four ferritic alumina-forming alloys were pre-oxidised before exposure to (Li,Na,K)$_2CO_3$-melt at 800 °C for 1000 h. Only outer transient alumina, such as γ-alumina, reacts with the melt, forming $LiAlO_2$. At the same time, the innermost α-Al_2O_3 scale remains intact. α-Al_2O_3, as well as α-$LiAlO_2$, are slow-growing compressive stress-stabilised oxide scales. Thus, the combined presence of α-Al_2O_3/α-$LiAlO_2$ improves the corrosion protection of materials investigated in this study, compared to non-pre-oxidised ones, by forming a superior double oxide scale.

1. Introduction

Thermal storage by employing molten salt is increasingly considered to minimise the time-dependency between energy conversion and utilisation for electricity production. In the case of concentrated solar power (CSP), for example, the thermal power of solar irradiation heats a heat transfer fluid (HTF) for immediate power generation or storage (Thermal Energy Storage – TES) for later on-demand electricity production. Molten salts are deployed as high-temperature HTFs and TES materials. Molten nitrates have been widely used as HTF and TES material for most commercial CSP plants and thermal energy storage in general [1]. Despite the International Energy Agency's goal for employing CSP plants to provide 11% of the world's electricity by 2050 [2], CSP plants still need to overcome many challenges to compete with other technologies [3].

The next generation of CSP plants (Gen3) aims to lower its cost per kilowatt hour by increasing its efficiency. Among the three proposed pathways for meeting the target goal, HTF/TES materials are required to collect and store solar energy at temperatures above 700–750 °C [4]. A commercial solar salt (60 $NaNO_3$:40 KNO_3 in wt%) is widely used in the currently operated CSP plants. Despite its desirable thermophysical properties, such as relatively low melting temperature, high storage capacity and thermal conductivity, it is thermally stable only up to 565 °C before decomposition [3,5]. Its limited thermal stability makes it necessary to find alternatives that can withstand high operating temperatures and function as HTF/TES materials. Among other candidates, molten carbonates have a good potential as HTF for Gen3 CSP. The ternary mixture of (32.1 Li_2CO_3, 33.4 Na_2CO_3 and - 34.5 K_2CO_3 in wt%) has a thermal stability of 670–1000 °C depending on the cover gas during exposure [5,6].

Another essential aspect that must be considered when choosing an HTF/ TES material is its compatibility with the metallic components in the CSP system. Corrosion-wise molten carbonates can lead to catastrophic plant failures due to their corrosive nature [7–9]. For the safe operation of CSP plants, metallic materials with tailored high corrosion resistance must be employed. In addition to utilising other corrosion mitigation techniques, such as purification processes for molten salt, applying high-temperature protective coatings, or heat treatment as pre-oxidation, several studies have been conducted to investigate the corrosion behaviour of different alloys [10].

A metal alloy is expected to form a thin, slow-growing, and adherent oxide scale that acts as a barrier to the environment to achieve acceptable corrosion behaviour. Numerous studies investigated the corrosion resistance of different alloys in contact with carbonate melts. Among the alloys studied are stainless steels, which form a chromia scale, and FeCrAl alloys or aluminide coatings growing an alumina scale [8–16].

However, at high temperatures, chromia scales failed to protect stainless steel against molten carbonates due to their dissolution by salt melts, resulting in internal oxidation and excessive carburisation. By contrast, alumina-forming alloys showed excellent corrosion resistance

* Corresponding author.
E-mail address: esraah@chalmers.se (E. Hamdy).

https://doi.org/10.1016/j.corsci.2023.111217
Received 16 January 2023; Received in revised form 21 April 2023; Accepted 23 April 2023
Available online 24 April 2023

against carbonate melts up to 800 °C [8,17,18].

Former studies investigated the interaction of alkali carbonates with alumina-forming alloys. It has been reported that lithium ions were the predominant and most active alkali species detected in growing oxides at high temperatures [8,12,19–21]. Based on the Lux-Flood acid-base concept [22,23], a base is an electron pair donor. The carbonate melt is a base producing O^{2-} upon decomposition, see Eq.1 [24]:

$$CO_3^{2-} = acid + O^{2-} \quad (1)$$

By arranging individual carbonate salts used in this study based on their self-dissociation, Li_2CO_3 has the highest basicity and activity. The dissociation species Li_2O also has the lowest solubility in binary alkali-carbonate combinations [25,26].

In our former work [17], we studied the corrosion behaviour of four ferritic alumina-forming alloys in contact with $(Li:Na:K)_2CO_3$ at 800 °C. The main findings showed a promising high corrosion resistance of the four selected ferritic alloys for at least a 1000 h exposure. Interestingly, a duplex oxide scale has been detected consisting of an inner α-$LiAlO_2$ scale and outer γ-$LiAlO_2$ crystals. In 1961, Lehmann and Hasselbarth published on the solid-state synthesis and characterisation of α- and γ-$LiAlO_2$ [27]. Hereby, reactants have been in powder form or supplied by the wet chemistry route. Their study investigated different parameters and conditions for transforming the two polymorphs. Upon the interaction of lithium carbonate with alumina powder, α-$LiAlO_2$ can be formed up to 747–777 °C before it converts to γ-$LiAlO_2$ [28–31].

In 1978, Evans et al. [32], working on zircaloy-1, reported the formation of a duplex oxide scale comprised of two zirconia polymorphs. Their study proposed that upon compressive stress, a stress-stabilised, tetragonal zirconia polymorph emerged at the metal/oxide interface, which subsequently relaxed to become a monoclinic lattice. Similarly, Byker et al. in 1979 proposed a Pressure-Temperature phase diagram for lithium aluminate, showing that the hexagonal α-$LiAlO_2$ phase could remain stable at a significantly higher temperature at increased pressure compared to its drive for phase transition into γ-LiAlO2 at ambient pressure [33].

In our previous publication [17], we adopted the stress-stabilised concept proposed by *Evans* et al. and *Byker* et al. [32,33], where an inner oxide layer, α-$LiAlO_2$, could form under compressive stress beneath another stress-relieved polymorph, γ-$LiAlO_2$. We concluded that the formation and growth of the thermodynamically unfavourable α-$LiAlO_2$ at 800 °C is due to the widening of the single-phase regime under compressive stresses [32–34].

Building on our former publication [17], selected ferritic alumina-forming alloys were in contact with $(Li,Na,K)_2CO_3$-melt at 800 °C. The investigated alloys grew $LiAlO_2$ scales and were categorised based on the formation and transformation of α- $LiAlO_2$ to γ-$LiAlO_2$ into "normal" and "deviating". "Normal" behaving alloys developed an α-$LiAlO_2$ scale without involving any ternary cationic species from the alloy. In contrast, the "deviating" behaving alloys develop a scale incorporating at least two cationic species from the bulk alloy.

In the present study, the same ferritic alumina forming alloys have been pre-oxidised in air at 1050 °C for 8 h before exposure to $(Li:Na:K)_2CO_3$ at 800 °C. In this case, no direct redox-coupling between the salt melt and the metal is expected. The question is whether the melt can react efficiently with alumina to arrive over time at the same behaviour observed for the non-pre-oxidised alloys, i.e., a slow-growing duplex α- and γ-$LiAlO_2$ scale at the alloy surface.

2. Experimental

Four ferritic alumina-forming alloys were selected for this study; see their nominal composition in Table 1. The four alloys have relatively similar aluminium content. Kanthal® APMT differs from Kanthal® AF chemical composition in Mo and Mn content. Kanthal® EF100 differ from Kanthal® EF101 in silicon content.

Tested metal coupons with initial measurements of 15 × 15 × 2 mm were ground and polished until 1 μm mirror-finished surfaces were obtained. Later, coupons were cleaned and dried using acetone and ethanol before being immersed in a salt mixture; see details of the corrosion testing procedure described in our former publication [35].

After cleaning, the polished metal coupons were pre-oxidised at 1050 °C for eight hours in lab air. Pre-oxidation step was conducted in a pre-heated standard Nabertherm box furnace LT 5/11. After pre-oxidation, samples were removed to air and left to cool to room temperature.

A ternary eutectic mixture of 32.1 wt% Li_2CO_3, 33.4 wt% Na_2CO_3 and - 34.5 wt% K_2CO_3 was prepared. The Li_2CO_3 (99.0%), Na_2CO_3 (99.9%), and K_2CO_3 (99.8%) salts were purchased from VWR chemicals, EMSURE anhydrous, and ThermoFisher Scientific, respectively. The salt mixture preparation procedure and impurities concentrations in each salt were summarised in [35].

The experimental setup used in this study was built specifically to ensure complete immersion of coupons in salt melts during exposures. The isothermal corrosion tests were conducted at 800 ± 5 °C under flowing CO_2. Each exposure produced two samples for each tested alloy. We assigned one sample for cross-section analysis, while the second was dedicated to surface analysis. Exposures were conducted for 500 h and 1000 h at 800 °C. Every 336 h, the experiment was paused and cooled to room temperature to refill the crucibles with salt; see [35]. Due to the necessity of rinsing the coupons with water after exposure completion for mass change measurements, each sample could only be measured once. For instance, after a 500 h exposure was completed, two coupons were retrieved from the setup for examination while two other samples remained until 1000 h had passed. Each weight change curve has four exposure time points, and each point has an error bar that is based on a minimum of eight measurements. Exposures were repeated at least twice.

2.1. Post-exposure surface analysis

Treatment of coupons produced from exposures differs based on the type of analysis needed. A metal coupon was rinsed with water according to the standard methods [36] and dedicated to mass change measurements, surface morphology investigation and X-ray diffraction (XRD) analysis. Samples were rinsed with distilled water at room temperature to remove the salt remnants; see the detailed rinsing procedure [35]. It is noteworthy to remind the reader that even though the rinsing procedure followed standard methods, water-soluble corrosion products could be lost [35,36]. Therefore, mass change values need to be treated carefully.

Scanning electron microscopy (SEM) and energy-dispersive X-ray spectroscopy (EDX) using a JEOL JSM-7800 F Prime or Phenom ProX Desktop SEM with an EDX detector were used for morphological analysis. Bruker D8 Discover XRD equipped with a Cu source, a secondary Si monochromator, and a point detector was employed for phase

Table 1
Nominal alloy composition (in weight percentage).

Alloy	Fe	Ni	Cr	Al	Si	Mn	Mo	Others
Kanthal®APMT	balance	–	21	5	0.7	0.4	3	RE; C 0.08
Kanthal® AF	balance	–	21	5.3	0.7	–	–	RE; C 0.08
Kanthal® EF101	balance	< 0.5	11–14	3.2–4.2	1.2	< 0.7	–	RE; C 0.08
Kanthal® EF100	balance	< 0.5	9.5–13	3.8–4.2	< 0.5	< 0.7	–	RE; C 0.08

identification.

2.2. Post-exposure cross-section analysis

No water rinsing for the tested coupons was applied for cross-section investigations. Instead, molten salt was poured out from alumina-crucibles at 500 °C after a completed exposure so that a coupon with a thin layer of remaining salts was obtained. This procedure enabled corrosion analysis without losing any corrosion products during the rinsing process, while no mass change data could be collected.

3. Results

To clearly illustrate the effect of pre-oxidation and non-pre-oxidised alumina-forming alloys, we compare the results with our previous publication [17].

3.1. Mass change measurements and XRD analyses of alumina forming alloys exposed to alkali carbonate melts

Mass change values of pre-oxidised alloys after exposure to (Li:Na:K)$_2CO_3$ are plotted in Fig. 1. As seen in Fig. 1a, a slight mass gain is observed over time for the three normally behaving alloys. Interestingly, pre-oxidation lowered the mass gain values significantly by comparing them with the mass change data of the non-pre-oxidised ones, Fig. 1b [17]. After 1000 h exposure, pre-oxidised Kanthal® APMT and EF101 have a lower mass gain than the non-pre-oxidised ones by a factor of ten and four for Kanthal® AF.

Unlike the normally behaving alloys, a slight mass loss was detected after 500 h and 1000 h exposures in Kanthal® EF100. It is also important to remind the reader that new coupons were used at each time interval; therefore, a slight deviation could be observed in the mass change values.

Before exposing the selected alloys to the carbonate melt, XRD analysis was performed to identify the phases formed upon pre-oxidation. The characteristic diffraction pattern of α-Al_2O_3 was detected after pre-oxidising Kanthal® APMT, AF and EF101 at 1050 °C for 8 h. Since the three normally behaving alloys show similar behaviour during exposure to the carbonate melt, Kanthal® APMT is selected to represent phases' evolution over time, see Fig. 2. Only α- and γ- Al_2O_3 are detected upon pre-oxidation, as shown in Fig. 2a. Kanthal® AF and EF101 showed stronger signals for transient alumina phases γ- Al_2O_3 and θ- Al_2O_3 and traces of $Al_2Fe_2O_6$ and $Al_{1.54}Cr_{0.46}O_3$, respectively. Unlike the three normally behaving alloys, no signals of a pure alumina scale were found in Kanthal® EF100. Instead, the main characteristic signals

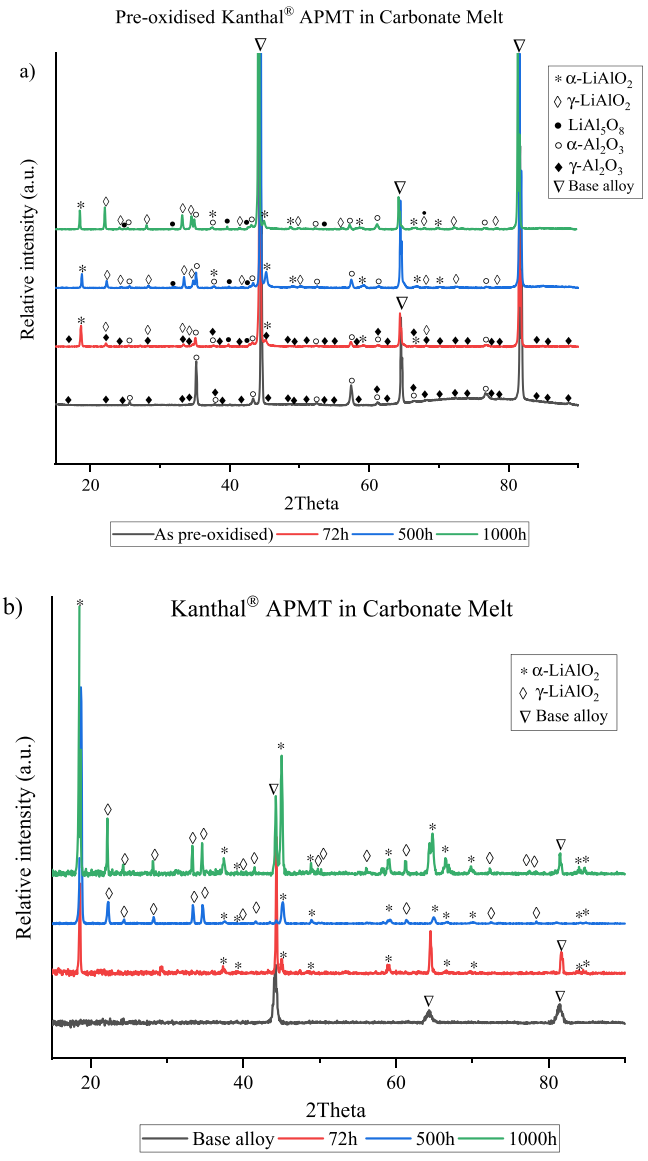

Fig. 2. Comparison of XRD diffractograms between a) pre-oxidised vs b) non-pre-oxidised Kanthal® APMT alloys immersed in alkali carbonate at 800 °C after different 72 h, 500 h and 1000 h.

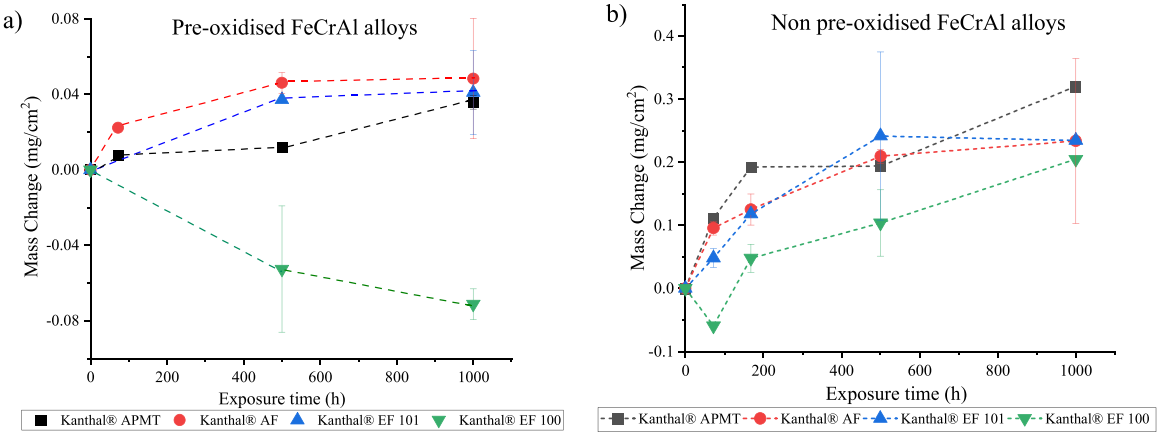

Fig. 1. Comparison of overall mass change behaviour between a) pre-oxidised vs b) non-pre-oxidised alumina forming alloys immersed in alkali carbonate at 800 °C after different exposure times [17]: (mass change values for pre-oxidised samples in (a) are approximately one order of magnitude lower than the non-pre-oxidised ones in (b).

detected correspond to $(Al_{0.9}Cr_{0.1})_2O_3$, $Al_{1.54}Cr_{0.46}O_3$, $FeAl_2O_4$, and $Fe_{0.9}Al_{1.1}O_3$.

After exposing Kanthal® APMT to the melt for 1000 h, the originally strong α-Al_2O_3 peaks start to weaken, and the peaks for α-$LiAlO_2$ and γ-$LiAlO_2$ phases become stronger. Interestingly, besides α-Al_2O_3, α-$LiAlO_2$ and γ-$LiAlO_2$, minor peaks of $LiAl_5O_8$ were detected for Kanthal AF and EF101 alloys; see Figures A and B in the supplementary files. Fig. 2a and b depicts a comparison of α-$LiAlO_2$ and γ-$LiAlO_2$ peak intensities for Kanthal® APMT between pre-oxidised vs non-pre-oxidised samples. In comparison, the time evolution of the diffraction pattern of the non-pre-oxidised samples presented a characteristic increase of α-$LiAlO_2$ and γ-$LiAlO_2$. In contrast, the pre-oxidised sample exhibits a stable α-$LiAlO_2$ signal.

3.2. Alloys forming α-/γ-$LiAlO_2$ upon reaction with Al_2O_3 scales in contact with Li_2CO_3

In our former publication [17], the investigated alloys were categorised upon their corrosion behaviour to "normal" and "deviating" formation and transformation of α-$LiAlO_2$. In this work, similar terminology is used, but the classification follows the reaction of alumina forming during pre-oxidation to lithium aluminates. Kanthal® APMT, Kanthal® AF and Kanthal® EF101 behave alike ("normal") by forming α-/γ-$LiAlO_2$ upon reaction with Al_2O_3 scales in contact with Li_2CO_3, whereas Kanthal® EF100 "deviates" in its reaction path by incorporating more than one metal ion from the bulk upon reaction with Li_2CO_3.

Fig. 3 shows the effect of the pre-oxidation on α-$LiAlO_2$ and γ-$LiAlO_2$ formation and growth. Fig. 3 is divided into four columns (1−4) and three rows (A-C). Colum no. 1 represents the surface morphology of "normal" behaving alloys after 1000 h exposure to the carbonate melt at 800 °C without pre-oxidation [17]. From our previous study, combing morphological analysis and XRD results, the smooth surface covered with small crystals were assigned as α-$LiAlO_2$ and the growing pyramidal crystals as γ-$LiAlO_2$. Column no. 2 depicts cross-section morphology after eight hours of pre-oxidation at 1050 °C and before exposure to carbonate melt. Finally, Columns no. 3 and 4 depict characteristic surface features of pre-oxidised coupons after being exposed to molten carbonate at 800 °C for 500 h and 1000 h, respectively.

In the case of pre-oxidation, mainly small crystals covering the surface were observed, as can be seen in Columns no. 3 and 4. The large characteristic crystals of γ-$LiAlO_2$, randomly distributed on the non-pre-oxidised samples (see A1, B1 and C1), did not form. Instead, as observed in B4 and C4, and in agreement with XRD results, tiny gamma γ-$LiAlO_2$ crystals started to nucleate and grow during the 1000 h of exposure. It is interesting to note the significant difference in the nucleation and growth rate of gamma lithium aluminate crystals between the absence and presence of pre-oxidation.Representative cross-sections of Kanthal® APMT samples illustrate the corrosion resistance of normally behaving alloys to salt melts over time, see Fig. 4. Comparing the surface morphology of the investigated alloys, the top view images in Fig. 3 Column 1 show the significantly larger γ-$LiAlO_2$ crystals in the absence of pre-oxidation. However, these characteristic crystals were not observed in the absence of pre-oxidation, Fig. 3 Columns 2–4. Even after 1000 h exposure of pre-oxidised alloys to alkali carbonates, Fig. 3 Column 4, γ-$LiAlO_2$ crystals were still absent. Interestingly, cross-section investigations for normally behaving alloys revealed the presence of three oxide layers, Fig. 4(a-c). Based on our former findings [17], we learned that stress-stabilised α-$LiAlO_2$ forms a dense and thin scale before nucleating stress-relaxed γ-$LiAlO_2$ crystals, as seen in Fig. 3 (A1, B1 and C1). Therefore, in agreement with XRD results and EDS point

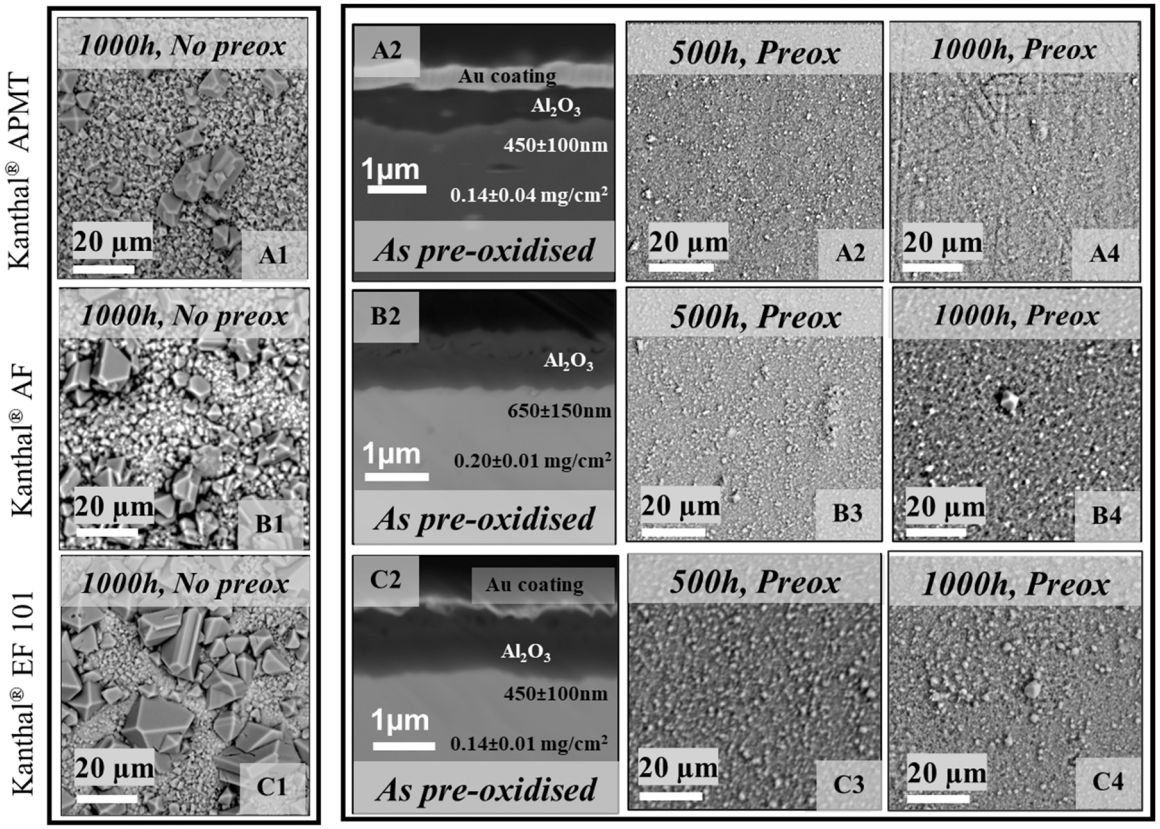

Fig. 3. SEM backscattered electron micrographs showing the cross-sections of "normally" behaving alloys after pre-oxidation and before salt exposures. Column 1 SEM backscattered images depict the surface morphology of non-pre-oxidised samples exposed to $(Li,Na,K)_2CO_3$-melts at 800 °C after 1000 h [17]. Columns 2–4: SEM backscattered electron micrographs showing the top view for pre-oxidised "normally" behaving alloys exposed to carbonate melts at 800 °C after 500 h and 1000 h at 800 °C.

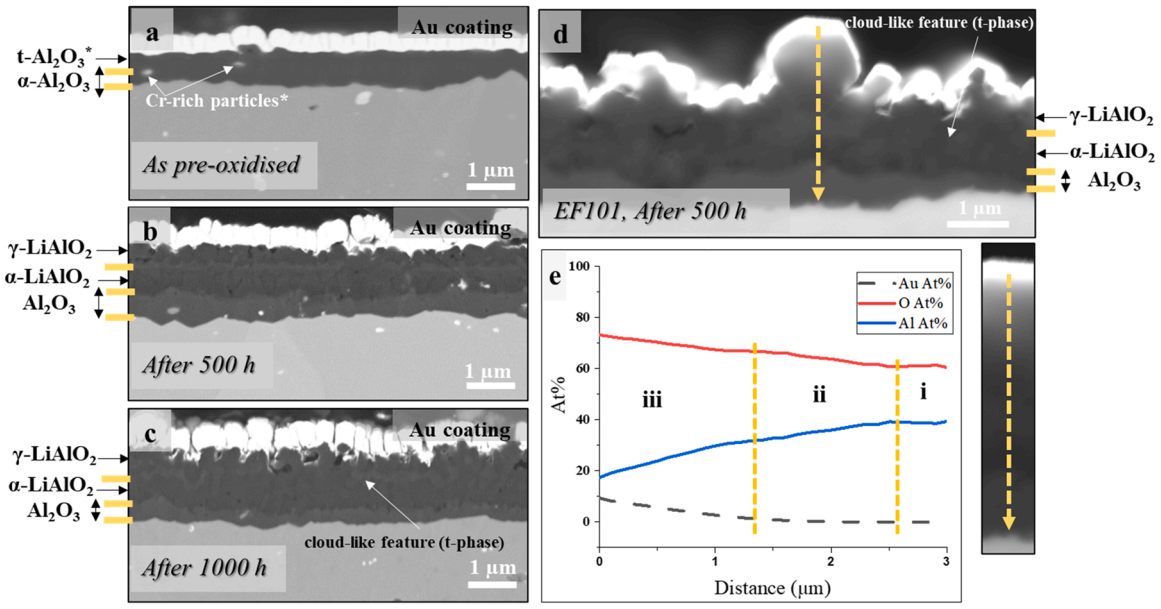

Fig. 4. cross-section scanning electron microscopic images of Kanthal® APMT a) after pre-oxidation for 8 h at 1050 °C, b) after 500 h, c) after 1000 h exposure to salt melt. An inhomogeneous cloud-like feature is observed within α/ γ-$LiAlO_2$ double layer. d) cross-section scanning electron microscopic image with a higher magnification of Kanthal® EF101 after 500 h exposure to alkali carbonate at 800 °C. e) an EDS line scan of oxide layers formed on (d).

analysis, the three-layered oxide scale is composed of γ-$LiAlO_2$ at the top, then beneath it α-$LiAlO_2$ and finally, an Al_2O_3 scale at the alloy-oxide interface. The latter Al_2O_3 scale has been absent in the case of the non-pre-oxidised samples. EDS point analyses for lithium aluminate polymorphs showed an approximate composition of ~33–35 at% Al and ~67–65 at% O. In comparison, the inner alumina scale has approximately 39–40 at% Al and 61–60 at% O. Based on the XRD results and EDS point analyses, we can conclude that lithium is the only participating species from the melt since no other alkali cationic species from the melt were detected.

Fig. 4d shows a higher magnification cross-section SEM image of Kanthal® EF101, another normally behaving alloy, after 500 h of immersion in the carbonate melt. Another interesting finding that can be seen in Fig. 4d is an inhomogeneous cloud-like feature with a difference in backscatter electron Z-contrast within the α/ γ-$LiAlO_2$ double layer, see Fig. 4c and d. An EDS line-scan analysis shown in Fig. 4e reveals a change in Al at% within these regions. Since detecting Li with the EDS analysis is not possible, we need to reconsider the at% measured in this case. The at% detected in zone (i) for oxygen and aluminium starts with ~60% and ~40% at the alloy oxide interface, indicating the presence of pristine Al_2O_3. The decrease of Al at% in zone (ii) corresponding with an increase in O at% indicates the formation of α-$LiAlO_2$ scale with an Al/O ratio of 33/66 at%. The trend of decreasing Al at% and increasing O at% in zone (iii) does not necessarily indicate increasing lithium; since the Au-sputter coating of the surface before cross-section stands for the element difference. In addition, XRD results reported the absence of potential highly lithiated phases, e.g. Li_5AlO_4, see Fig. 2a. The only Li-aluminate phases detected in the XRD diffractograms are α-$LiAlO_2$, γ-$LiAlO_2$ and $LiAl_5O_8$.

Fig. 5 represents the thickness evolution over time for pre-oxidised vs non-pre-oxidised of the normally behaving alloy Kanthal® APMT. After 1000 h exposure, the overall oxide scale thicknesses of the pre-oxidised alloys were significantly lower than the non-pre-oxidised samples. What was surprising here was the thickness evolution of the three layers over time. As seen in Fig. 5, the alumina scale formed during pre-oxidation is getting thinner over time. After 1000 h, almost 50–60% of the Al_2O_3 layer was consumed or reacted with the salt melts, forming lithiated species. On the other hand, α-$LiAlO_2$ scale and γ-$LiAlO_2$ crystals were slowly growing. Furthermore, the inner scale (α-Al_2O_3) of the pre-

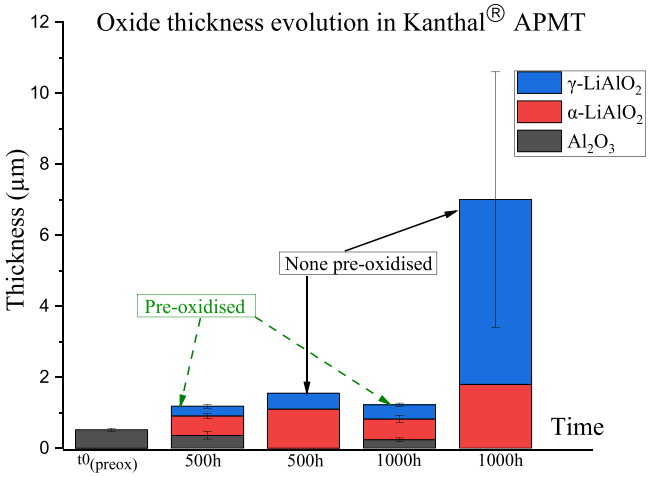

Fig. 5. Oxide thickness evolution over time for pre-oxidised vs non-pre-oxidised Kanthal® APMT after exposure to $(Li,Na,K)_2CO_3$-melts at 800 °C.

oxidised samples remains intact in thickness. Thus, combing these summarising results with the measured mass change values, pre-oxidised Kanthal® APMT has a lower mass gain by a factor of 10 compared to non-pre-oxidised one and by a factor of 10^3 to a chromia-forming austenitic stainless steel which was investigated in our former study under the same conditions [8].

3.3. Alloys incorporating more than one metal ion from the bulk upon reaction with Li_2CO_3

The XRD diffractogram of Kanthal® EF100 after pre-oxidation and before exposure to salt melt (Fig. 6) shows a solid solution of mixed oxides. Unlike the three normally behaving alloys, no signal for any pure alumina phase was found on pre-oxidised Kanthal® EF100. Instead, the main characteristic phases detected were $(Al_{0.9}Cr_{0.1})_2O_3$, $Al_{1.54}Cr_{0.46}O_3$, $FeAl_2O_4$, and $Fe_{0.9}Al_{1.1}O_3$. Interestingly, after a 1000 h exposure to (Li:Na:K)$_2CO_3$, signals of these mixed oxides disappear altogether, and a signal from an aluminium-rich iron oxide $Al_{1.93}Fe_{0.07}O_3$ was detected. In

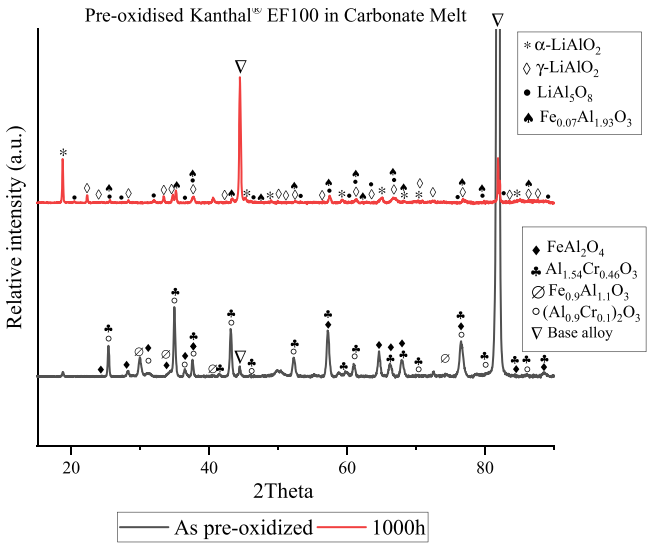

Fig. 6. XRD diffractograms of a pre-oxidised Kanthal® EF100 before and after 1000 h exposure to alkali carbonate at 800 °C.

addition, signals of α-$LiAlO_2$ and γ-$LiAlO_2$ appeared.

Fig. 7a shows a cross-section SEM image of Kanthal® EF100 after being pre-oxidised at 1050 °C for 8 h. The cross-section analysis shows inwards growing mixed oxides with an average thickness of 1400 ± 500 nm. The upper and middle parts of the oxide formed are composed of Fe-Al, and Fe-Cr-Al mixed oxides, while the lower zone has an Al-rich oxide scale. Pegs were also developed in the sub-oxide region, reaching ~5.7 μm deep into the alloy and filled with mixed oxides. EDS point analyses show that Al-Fe-Cr mixed oxide has an average chemical composition: O ~60 at%, Al (29–33 at%), Fe (6–11 at%), and Cr < 3 at %.

After 500 h exposure to the $(Li,Na,K)_2CO_3$ melt, a duplex layer was observed with a denser compact inner scale and an outer porous zone, Fig. 7b. Most iron and chromium ions have vanished from the oxide scale. Pores can indicate a leaching process of ions from the outer oxide scale by the melt. The presence of these voids can partially explain the mass loss detected in Kanthal® EF100; see Fig. 1a.

Interestingly, after 1000 h and as shown in Fig. 7c, Kanthal® EF100 seems to develop an inner aluminium-rich scale that is compact, dense and adherent with a 900 ± 400 nm thickness. In contrast, the outer oxide layer, composed of lithiated oxide species with an average thickness of 600–1200 nm, did not adhere to the inner scale, which partially explains the mass loss.

4. Discussion

4.1. Alloys forming α-/γ-$LiAlO_2$ upon reaction with Al_2O_3 scales in contact with Li_2CO_3

The pre-oxidation of alumina-forming alloys at 1050 °C formed α-alumina as well as transient γ- and θ-alumina scales on Kanthal® AF, APMT and EF101 and other alumina-forming FeCrAls [37–40]. EF100 formed a mixed oxide and will be discussed later in the discussion.

Upon exposing these pre-oxidised alloys to molten carbonates, transient γ- and θ-alumina react rapidly with Li- and O-ions from the salt melt, producing mainly α-$LiAlO_2$. Worth mentioning that Li_2CO_3 decomposes in contact with the alumina surface into Li- and O-ions and CO_2(g), which in short, means that Li_2O is the only participating species from the melt in the growing scale, see Eq. 2. After 500 h, the only alumina signal detectable via XRD originates from the α-Al_2O_3 structure. All other signals match only lithium aluminates. The initial rapid but low mass gain reflects a 40% mass increase caused by the following reaction:

$$transient \quad Al_2O_3 + Li_2O \rightarrow 2LiAlO_2 \tag{2}$$

After completion of the transient alumina reaction with Li_2O to $LiAlO_2$, the mass change curve flattens drastically. In fact, due to

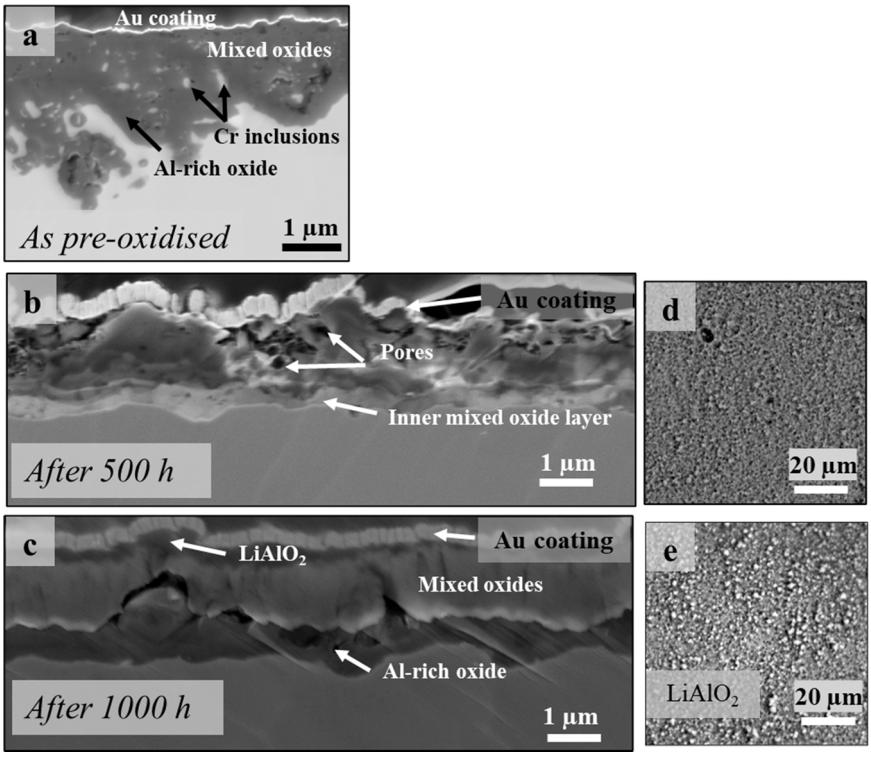

Fig. 7. cross-section scanning electron microscopic images of Kanthal® EF100 a) after pre-oxidation for 8 h at 1050 °C, b) after 500 h, c) after 1000 h exposure to salt melt. Top view scanning electron microscopic images d) after 500 h, e) after 1000 h exposure to $(Li,Na,K)_2CO_3$ melt.

measurement fluctuations resulting from the rinsing procedure, the mass change kinetics is so low that it could point both ways within the uncertainty values of the method. Thus, we need to consider very slow transport processes leading towards oxidation or dissolution.

The most decisive reaction is the transformation of transient alumina into α-$LiAlO_2$. Our former study [17] shows that α-$LiAlO_2$ is a stress-stabilised polymorph occurring in the form of a uniform and dense inner scale at 800 °C on Kanthal® AF, APMT and EF101 if no pre-oxidation has been performed prior to the exposure in the molten carbonate melt. In the pre-oxidised case, the stress stabilisation is provided by a substantial swelling (Pilling Bedworth) of the transient alumina upon Li_2O uptake. The compressed α-$LiAlO_2$ is an acting sealant that decreases significantly further ions' transport towards the underlying α-Al_2O_3 scale. Interrogating the pseudo-binary phase diagram in Fig. 8 further towards lean lithium ratios, one finds lithium pentaaluminate, $LiAl_5O_8$. Traces of $LiAl_5O_8$ have indeed been shown in XRD spectra of Kanthal® APMT (see image 2a), and in EF101 and Kanthal® AF; see Figures A and B in the supplementary files. A powder synthesis study by Eremina et al. demonstrates in a dedicated study that the $LiAl_5O_8$ formation from γ-Al_2O_3 and Li_2CO_3 reactants depends on the γ-Al_2O_3 powder grain size and even more so on mechanical milling, rather than on variation of the synthesis temperature [41]. Larger γ-Al_2O_3 grains without additional mechanical treatment showed $LiAlO_2$ as the dominant product, which resembles the oxide scale formed on the samples in the current study. In this context, $LiAl_5O_8$ is a transient product upon lithiation of the pre-oxidised alumina scale.

The resulting double oxide scale α-Al_2O_3/α-$LiAlO_2$ brings further

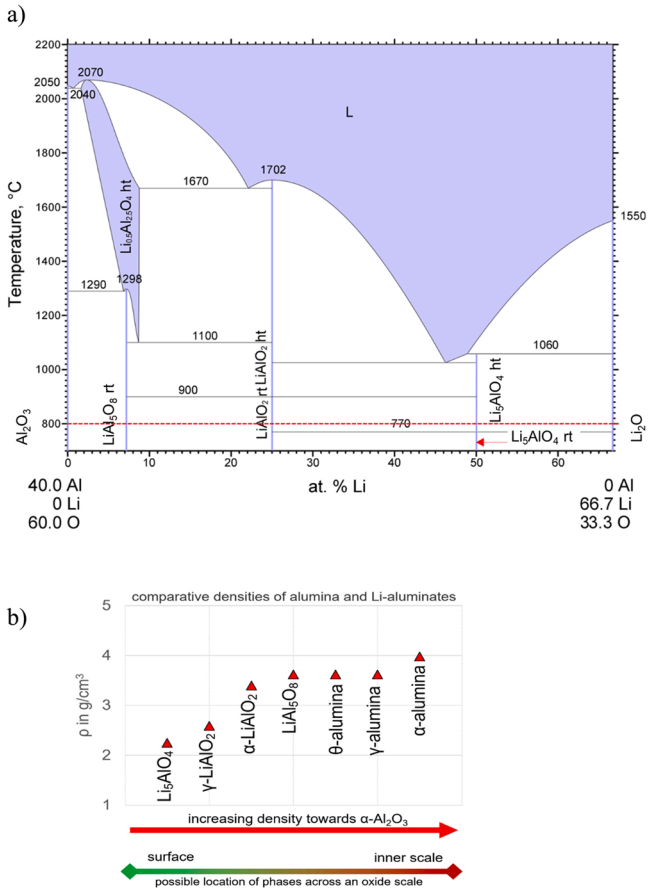

Fig. 8. Left: Pseudo-binary phase diagram for Al_2O_3-Li_2O as a function of at% Li [42]. The red dashed line highlights 800 °C and crosses three stable Li-aluminate phases—right: plot showing the densities of different alumina crystal structures and Li-aluminates. The data was obtained from Springer Materials [37,43–49].

oxidation almost to a halt.

To test this hypothesis, predicting the maximum mass gain by Li_2O uptake of a pre-oxidised FeCrAl alloy should be possible by inspecting the alumina scale's α- to γ-Al_2O_3 ratio prior to exposure to the alkali carbonate melt. Table 2 presents an example calculation for a sample with a 450 nm thick alumina scale after pre-oxidation (agreeing with our initial scale thickness), comprising 1/3 α- and 2/3 γ-alumina. In this example, only the γ-Al_2O_3 reacts with Li_2O to form α-$LiAlO_2$ and causes the initial mass gain while α-$LiAlO_2$ remains intact.

Comparing this estimate with the mass gain results presented in Fig. 1a, it matches quite precisely the expectation value, not to exceed more than 0.04 mg/cm^2, independent of exposure time as long as the inner α-alumina scale is intact. This exercise confirmed that the performance of pre-oxidised alumina formers in lithium carbonate comprising melts is highly dependent on the duration and temperature of the pre-oxidation process since transient to α-Al_2O_3 ratios have been shown to be sensitive to those parameters in several studies in the literature [40,50,51].

After discussing the inwards transport of lithium and oxygen ions by the reaction with transient alumina, it is necessary to reflect also on the possibility of an ongoing transformation of α-$LiAlO_2$ to γ-$LiAlO_2$ or further reaction with lithium carbonate to higher lithiated aluminates, e.g. Li_5AlO_4 (Fig. 8a [42]). The XRD signal for γ-$LiAlO_2$ is indeed slightly increasing over time. However, the higher lithiated structure Li_5AlO_4 was not observed; this is not disproving its formation since it might have been taken into the melt flux. However, studies by Lehmann et al. showed that it requires Li_2O rather than Li_2CO_3 to stabilise the highly lithiated structure [52].

If we discuss this behaviour to its extreme and all α-$LiAlO_2$ is eventually transformed into non-protective γ-$LiAlO_2$ and Li_5AlO_4, α-alumina acts as the protective interface between melt and alloy. α-alumina possesses the highest density of the here-discussed oxidised structures (Fig. 8b). Thus, the resistance towards lithium uptake and the corresponding Pilling-Bedworth effect is expected to be high.

Therefore, it can be said that pre-oxidation and exposure of the alumina formers Kanthal® AF, APMT and EF101 exhibit the highest possible protection of the alloy via the formation of an α-Al_2O_3/α-$LiAlO_2$ double scale, both very slow growing. A simplified schematic of our observations is shown in Fig. 9.

4.2. Alloys incorporating more than one metal ion from the bulk upon reaction with Li_2CO_3

Kanthal® EF100, on the other hand, exhibits mass loss. This can be explained by analysing the phases formed by its pre-oxidation. Iron and chromium ions are present in the inhomogeneous aluminium-rich oxide scale. Those ions can be leached by molten carbonates, leaving a porous oxide scale behind. However, after 1000 h, EDX *point analysis (~40% Al and ~60% O)* and XRD results show a nearly pristine inner alumina-rich scale. Mass loss can also partially be explained by the spallation of the mixed oxides layer, as observed in Fig. 7c. It is unclear how the inner aluminium-rich oxide underneath the leached oxide regions can perform for long-term exposures beyond 1000 h. Deceleration of the mass loss

Table 2
Mass change estimation of a pre-oxidised alumina-forming alloy after reacting with Li-carbonate.

alumina scales after pre-oxidation	thickness min. [nm]	density g/cm^3	m (oxide) after pre-oxidation [mg/cm^2]	max. mass gain in carbonates [mg/cm^2]
total Al_2O_3	450		0.17	0.04 (total mass gain)
(2/3) γ-Al_2O_3	300	3.62	0.11	0.04 (α-$LiAlO_2$ via Eq.1)
(1/3) α-Al_2O_3	150	3.98	0.06	0

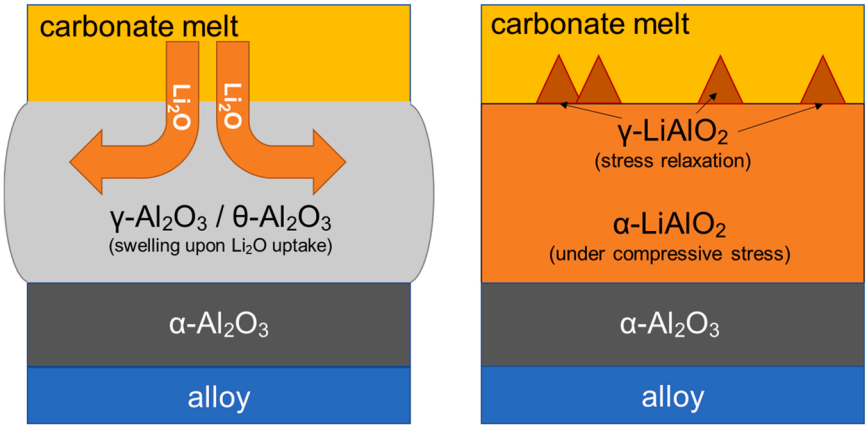

Fig. 9. – Schematic summary for phase transitions occurring on pre-oxidised alumina forming alloys exposed to lithium ion-containing alkali carbonate melts at 800 °C on the condition that a dense and pristine inner alumina scale has been achieved upon pre-oxidation. The uptake of lithium and oxygen ions upon the reaction with transient aluminas causes stresses due to swelling. This allows for the formation of the stress-stabilised α-$LiAlO_2$ on top of the inner α-Al_2O_3. Partial stress relaxation is provided by γ-$LiAlO_2$ formation at the melt/oxide interface.

appears promising.

5. Summary

1. Forming an inner α-Al_2O_3 scale, upon pre-oxidising ferritic FeCrAl alloys decelerates the corrosion caused by alkali carbonate melts further compared to previously reported non-pre-oxidised FeCrAl alloys.
2. Outer transient alumina scales formed during a pre-oxidation process react with lithium carbonate, forming the stress-stabilised α-$LiAlO_2$ on top of the inner α-alumina scale, providing an additional protective oxide scale.
3. Consequently, the quality and thickness of a protective α-Al_2O_3/α-$LiAlO_2$ is defined by the α-/transient- alumina ratio, which in term depends on the alloy's chemical composition.
4. Secondary cations in the oxide scale, chromium or iron ions, observed for pre-oxidised Kanthal® EF100 leach into the alkali carbonate melt upon exposure. This leaching process causes a temporary mass loss, which comes to a halt when a nearly pure aluminium oxide scale has formed at the alloy/oxide interface.

CRediT authorship contribution statement

Esraa Hamdy: Conducting exposure experiments, sample analyses, main author of this article. **Fang Liu:** sample analyses, co-authoring, reviewing and editing co-authoring this article. **Christine Geers:** sample analyses, co-authoring, reviewing and editing this article.

Declaration of Competing Interest

The authors declare the following financial interests/personal relationships which may be considered as potential competing interests: Christine Geers reports financial support was provided by Swedish Energy Agency.

Data Availability

Data will be made available on request.

Acknowledgements

This work has been financially supported by the Research and Research Education Committee at Chemistry and Chemical Engineering Department, Chalmers University of Technology. Part of the work has received funding from High-Temperature Corrosion (HTC) Centre via Swedish Energy Agency within the thermal storage for SOLEL initiative under contract number 44653-1 (2017–2021).

Appendix A. Supporting information

Supplementary data associated with this article can be found in the online version at doi:10.1016/j.corsci.2023.111217.

References

[1] N. Breidenbach, C. Martin, H. Jockenhöfer, T. Bauer, Thermal energy storage in molten salts: overview of novel concepts and the DLR test facility TESIS, Energy Procedia 99 (2016) 120–129.
[2] IEA. Technology roadmap - concentrating solar power IEA Paris 2010.
[3] A. Caraballo, S. Galán-Casado, Á. Caballero, S. Serena, Molten salts for sensible thermal energy storage: a review and an energy performance analysis, Energies 14 (2021) 1197.
[4] M. Mehos, C. Turchi, J. Vidal, M. Wagner, Z. Ma, C. Ho, W. Kolb, C. Andraka, A. Kruizenga, Concentrating solar power gen3 demonstration roadmap, Natl. Renew. Energy Lab. (2017).
[5] L. Ma, C. Zhang, Y. Wu, Y. Lu, Comparative review of different influence factors on molten salt corrosion characteristics for thermal energy storage, Sol. Energy Mater. Sol. Cells 235 (2022), 111485.
[6] K. Vignarooban, X. Xu, A. Arvay, K. Hsu, A.M. Kannan, Heat transfer fluids for concentrating solar power systems - a review, in: Applied Energy, Elsevier Ltd, 2015, pp. 383–396.
[7] P. Audigié, S. Rodríguez, A. Agüero, F. Pedrosa, T. Paiva, T.C. Diamantino, Comparison of descaling methods to study the corrosion kinetics of ferritic steels after dynamic exposure to molten carbonates, Corros. Sci. 209 (2022), 110786.
[8] E. Hamdy, J. Nockert-Olovsjö, C. Geers, Perspectives on selected alloys in contact with eutectic melts for thermal storage: nitrates, carbonates and chlorides, Sol. Energy 224 (2021) 1210–1221.
[9] E. Hamdy, A. Wagné, C. Geers, Evaporated alkali carbonate effect on an aluminum diffusion coated 253MA vessel after 4000h discontinuous operation-lessons learned, Energies 15 (2022) 3241.
[10] X. Song, G. Zhang, H. Tan, L. Chang, L. Cai, G. Xu, Z. Deng, Z. Han, Review on thermophysical properties and corrosion performance of molten salt in high temperature thermal energy storage, IOP Conf. Ser.: Earth Environ. Sci. 474 (2020), 052071.
[11] C. Prieto, S. Fereres, F.J. Ruiz-Cabañas, A. Rodriguez-Sanchez, C. Montero, Carbonate molten salt solar thermal pilot facility: plant design, commissioning and operation up to 700 °C, Renew. Energy 151 (2020) 528–541.
[12] M. Spiegel, P. Biedenkopf, H.J. Grabke, Corrosion of iron base alloys and high alloy steels in the Li2CO3-K2CO3 eutectic mixture, Corros. Sci. 39 (1997) 1193–1210.
[13] S. Ahn, K. Oh, M. Kim, J. Youn, K. Jo, K. Kim, H. Kwon, Electrochemical analysis on the growth of oxide formed on stainless steels in molten carbonate at 650 °C, Int. J. Hydrog. Energy 39 (2014) 12291–12299.
[14] S.P. Sah, E. Tada, A. Nishikata, Corrosion behaviour of austenitic stainless steels in carbonate melt at 923 K under controlled CO_2-O2 environment, in: Corrosion Science, Elsevier Ltd, 2018, pp. 310–317.
[15] M. Sasaki, S. Ohta, N. Igata, Influence of the alloying elements of the stainless steels on the corrosion behavior in molten carbonate, Zair. -to-Kankyo 45 (1996) 192–200.
[16] P. Audigié, V. Encinas-Sánchez, S. Rodríguez, F.J. Pérez, A. Agüero, High temperature corrosion beneath carbonate melts of aluminide coatings for CSP application, Sol. Energy Mater. Sol. Cells 210 (2020), 110514.
[17] E. Hamdy, M. Strach, J. Nockert-Olovsjö, C. Geers, Differentiation in corrosion performance of alumina forming alloys in alkali carbonate melts, Corros. Sci. (2021), 109857.
[18] A.G. Fernández, F. Pineda, M. Walczak, L.F. Cabeza, Corrosion evaluation of alumina-forming alloys in carbonate molten salt for CSP plants, Renew. Energy 140 (2019) 227–233.

[19] K. Takeuchi, A. Nishijima, K. Ui, N. Koura, C.K. Loong, Corrosion behavior of Fe-Cr alloys in Li2CO3-K2CO3 molten carbonate, J. Electrochem. Soc. 152 (2005) B364–B368.

[20] M. Spiegel, P. Biedenkopf, H.-J. Grabke, Corrosion of iron base alloys and high alloy steels in the Li2CO3-K2CO3 eutectic mixture, Corros. Sci. 39 (1997) 1193–1210.

[21] S. Frangini, S. Loreti, The role of temperature on the corrosion and passivation of type 310S stainless steel in eutectic (Li + K) carbonate melt, J. Power Sources (2006) 800–804.

[22] H. Lux, "Säuren" und "Basen" im Schmelzfluss: die bestimmung der sauerstoffionen-konzentration, Z. für Elektrochem. und Angew. Phys. Chem. 45 (1939) 303–309.

[23] H. Flood, T. Forland, K. Motzfeld, On the oxygen electrode in molten salts, Acta Chem. Scand. 6 (1952) 257–269.

[24] P. Wang, Y. Zhang, H. Shi, P. Li, K. Du, H. Yin, D. Wang, Local basicity dependent gas-liquid interfacial corrosion of nickel anode and its protection in molten Li2CO3-Na2CO3-K2CO3, J. Electrochem. Soc. 169 (2022), 031505.

[25] S. Frangini, Lux-flood basicity of mixed La2O3-alkali molten carbonates determined by analysis of their oxygen solubility properties, Open Phys. Chem. J. 3 (2009).

[26] M. Cassir, G. Moutiers, J. Devynck, Stability and characterization of oxygen species in alkali molten carbonate: a thermodynamic and electrochemical approach, J. Electrochem. Soc. 140 (1993) 3114.

[27] H.-A. Lehmann, H. Hesselbarth, Zur Kenntnis der Lithiumaluminate. I. Über eine neue Modifikation des LiAlO2, Z. für Anorg. und Allg. Chem. 313 (1961) 117–120.

[28] V. Danek, M. Tarniowy, L. Suski, Kinetics of the α → γ phase transformation in LiAlO2 under various atmospheres within the 1073–1173 K temperatures range, J. Mater. Sci. 39 (2004) 2429–2435.

[29] S.J. Heo, B. Hu, M.A. Uddin, A. Aphale, A. Hilmi, C.-Y. Yuh, A. Surendranath, P. Singh, Role of exposure atmospheres on particle coarsening and phase transformation of LiAlO2, J. Electrochem. Soc. 164 (2017) H5086–H5092.

[30] M.J. Bennett, R. Newton, J.R. Nicholls, The behaviour of commercial FeCrAlRE alloys in nitrogen-oxygen - water vapour bioxidant environments, Mater. High. Temp. 20 (2003) 347–356.

[31] H.J. Choi, J.J. Lee, S.H. Hyun, H.C. Lim, Phase and microstructural stability of electrolyte matrix materials for molten carbonate fuel cells, fuel cells 10 (2010) 613–618.

[32] H.E. Evans, D.J. Norfolk, T. Swan, Perturbation of parabolic kinetics resulting from the accumulation of stress in protective oxide layers, J. Electrochem. Soc. 125 (1978) 1180–1185.

[33] H.J. Byker, I. Eliezer, N. Eliezer, R.A. Howald, Calculation of a phase diagram for the lithium oxide-aluminum oxide (LiO0.5-AlO1.5) system, J. Phys. Chem. 83 (1979) 2349–2355.

[34] P. Bouvier, E. Djurado, G. Lucazeau, T. Le Bihan, High-pressure structural evolution of undoped tetragonal nanocrystalline zirconia, Phys. Rev. B 62 (2000) 8731–8737.

[35] E. Hamdy, J. Nockert-Olovsjö, C. Geers, Addit. Data Exp. setups Use Study Alloy. Contact High. Temp. eutectic melts Therm. Storage Data Brief. (2021), 107446.

[36] Standard Practice for Preparing, Cleaning, and Evaluating Corrosion Test Specimens, in: Methods for Cleaning After Testing (ASTM G1–03 (2017)e1), © ASTM International, 2017.

[37] S. Yoneda, S. Hayashi, Effect of Cr content on microstructure and growth of external Al2O3 scale formed on Fe–Cr–Al alloys, Oxid. Met. 97 (2022) 195–208.

[38] F. Liu, Microstructural investigation of high temperature oxidation of Al2O3-forming and Cr2O3-forming steels - The influence of water vapour, in: Applied Physics, Microscopy and Microanalysis, Chalmers University of Technology, Gothenburg, 2008.

[39] L. Kovarik, M. Bowden, J. Szanyi, High temperature transition aluminas in δ-Al2O3/θ-Al2O3 stability range: review, J. Catal. 393 (2021) 357–368.

[40] G. Berthomé, E. N'Dah, Y. Wouters, A. Galerie, Temperature dependence of metastable alumina formation during thermal oxidation of FeCrAl foils, Materials and Corrosion 56 (2005) 389–392.

[41] N.V. Eremina, V.P. Isupov, Mechanochemical synthesis of lithium pentaaluminate from lithium carbonate and boehmite, Inorg. Mater. 56 (2020) 466–472.

[42] Al-Li-O Vertical Section of Ternary Phase Diagram: Datasheet from "PAULING FILE Multinaries Edition – 2012. in SpringerMaterials https://materials.springer.com/isp/phase-diagram/docs/c_1100990), in: P. Villars, H. Okamoto (Eds.), Springer-Verlag Berlin Heidelberg & Material Phases Data System (MPDS), Switzerland & National Institute for Materials Science (NIMS), Japan.

[43] α-Li5AlO4 (Li5AlO4 rt) Crystal Structure: Datasheet from "PAULING FILE Multinaries Edition – 2012. in SpringerMaterials https://materials.springer.com/isp/crystallographic/docs/sd_1011784), in: P. Villars, K. Cenzual (Eds.), Springer-Verlag Berlin Heidelberg & Material Phases Data System (MPDS), Switzerland & National Institute for Materials Science (NIMS), Japan.

[44] γ-LiAlO2 (LiAlO2 ht) Crystal Structure: Datasheet from "PAULING FILE Multinaries Edition – 2012. in SpringerMaterials (https://materials.springer.com/isp/crystallographic/docs/sd_0382052), in, Springer-Verlag Berlin Heidelberg & Material Phases Data System (MPDS), Switzerland & National Institute for Materials Science (NIMS), Japan.

[45] α-LiAlO2 (LiAlO2 rt) Crystal Structure: Datasheet from "PAULING FILE Multinaries Edition – 2012. in SpringerMaterials (https://materials.springer.com/isp/crystallographic/docs/sd_0382051), in, Springer-Verlag Berlin Heidelberg & Material Phases Data System (MPDS), Switzerland & National Institute for Materials Science (NIMS), Japan.

[46] Li0.5Al2.5O4 (LiAl5O8 rt) Crystal Structure: Datasheet from "PAULING FILE Multinaries Edition – 2012. in SpringerMaterials ⟨(https://materials.springer.com/isp/crystallographic/docs/sd_0313676)⟩, in: P. Villars, K. Cenzual (Eds.), Springer-Verlag Berlin Heidelberg & Material Phases Data System (MPDS), Switzerland & National Institute for Materials Science (NIMS), Japan.

[47] γ-Al2O3 (Al2.67O4 m-γ tet) Crystal Structure: Datasheet from "PAULING FILE Multinaries Edition – 2012. in SpringerMaterials ⟨(https://materials.springer.com/isp/crystallographic/docs/sd_1800435)⟩, in: P. Villars, K. Cenzual (Eds.), Springer-Verlag Berlin Heidelberg & Material Phases Data System (MPDS), Switzerland & National Institute for Materials Science (NIMS), Japan.

[48] θ-Al2O3 (Al2O3 m-θ) Crystal Structure: Datasheet from "PAULING FILE Multinaries Edition – 2012. in SpringerMaterials (https://materials.springer.com/isp/crystallographic/docs/sd_1800434), in: P. Villars, K. Cenzual (Eds.), Springer-Verlag Berlin Heidelberg & Material Phases Data System (MPDS), Switzerland & National Institute for Materials Science (NIMS), Japan.

[49] α-Al2O3 (Al2O3) Crystal Structure: Datasheet from "PAULING FILE Multinaries Edition – 2012. in SpringerMaterials ⟨()https://materials.springer.com/isp/crystallographic/docs/sd_0315064), in: P. Villars, K. Cenzual (Eds.), Springer-Verlag Berlin Heidelberg & Material Phases Data System (MPDS), Switzerland & National Institute for Materials Science (NIMS), Japan.

[50] S. Chevalier, A. Galerie, O. Heintz, R. Chassagnon, A. Crisci, Thermal alumina scales on FeCrAl: characterization and growth mechanism, Mater. Sci. Forum, Trans. Tech. Publ. (2008) 915–922.

[51] R. Chegroune, E. Salhi, A. Crisci, Y. Wouters, A. Galerie, On the competitive growth of alpha and transient aluminas during the first stages of thermal oxidation of FeCrAl alloys at intermediate temperatures, Oxid. Met. 70 (2008) 331–337.

[52] H.-A. Lehmann, H. Hesselbarth, Über das Li5AlO4, Z. für Anorg. und Allg. Chem. 315 (1962) 14–18.